



Lake Ice Thickness retrieval using TanDEM-X immediate interferometry

Peilin Chen¹, Grant Gunn¹, Sukhdip Kharoud¹

¹Department of Geography and Environmental Management, University of Waterloo, Waterloo, N2L 3G1, Canada

5 *Correspondence to:* Peilin Chen (peilin.chen1@uwaterloo.ca)

Abstract. Knowledge of Lake Ice Thickness (LIT) is essential for understanding the cryosphere and monitoring current climate change impacts. However, accurately retrieving LIT at the desired spatial-temporal scale remains a challenge, as many lakes are in remote regions and LIT is a logistically expensive parameter to measure. Interferometric synthetic aperture radar (InSAR) provides a novel approach to estimating ice thickness by measuring surface deformations at high resolution.

10 This study used TanDEM-X pursuit mode that offers minimal temporal correlation to maintain high coherence for accurate LIT retrieval in thermokarst lakes in Northern Alaska during the 2014-2015 winter season. The InSAR-derived LIT was validated against simulations from the Canadian Lake Ice Model (CLIMo), supported by in-situ snow and ice measurements. Results show consistent ice growth patterns and an RMSE of 0.08–0.26 m, demonstrating that the proposed method captures LIT evolution with reasonable agreement with CLIMo estimates. By employing an immediate interferometric approach, the
15 present study maintains sufficient coherence to isolate and highlight the influence of volume scattering, which shifts the phase center away from the ice-water interface, and is the main factor limiting the accuracy of the LIT retrieval. These findings provide new insights into the technology of InSAR-derived LIT and suggest that SAR missions operating at longer wavelengths, such as NISAR and TanDEM-L, hold significant potential for improving retrieval accuracy by enhancing penetration and reducing sensitivity to internal scattering within the ice volume.

20 1 Introduction

Lake ice thickness (LIT) is a crucial parameter for cryosphere studies and climate change monitoring (Brown & Duguay, 2010). Lake ice supports habitable lake ecosystems (Hampton et al., 2017; Ozersky et al., 2025), reacts to climate variability (Brown & Duguay, 2010), and has a socioeconomic impact on nearby communities (Perrin et al., 2015). The World Meteorological Organization's Global Climate Observation System (GCOS) regards LIT as a critical requirement for climate
25 change monitoring, as the primary drivers for ice development are air temperature and snow depth (GCOS, 2022). Consistent monitoring of LIT is logistically costly to conduct manually for many remote lakes, making it difficult to accurately retrieve LIT in Arctic regions at the desired spatial-temporal scale (Murfit & Duguay, 2021). The decline in manual meteorological observation networks is currently posing increasing challenges to the LIT retrieval (Vincent et al., 2012). As a result, the most common approach for LIT monitoring in contemporary research is the use of remote sensing technology (Duguay et al.,
30 2015).



The majority of techniques for LIT retrieval use active remote sensing devices, such as Synthetic Aperture Radar (SAR), which can penetrate cloud cover and the atmosphere-ice interface (Murfit & Duguay, 2021). Since ice and air have relatively similar dielectric characteristics, SAR signals can pass through the air-ice interface and are reflected at the ice-water layer due to the greater dielectric contrast (Hallikainen, 1977). In the early stages of primary ice formation, the thin, smooth ice layer exhibits backscatter characteristics similar to those of calm water, where specular scattering predominates and results in low backscatter (Duguay et al., 2002; Pietroniro & Leconte, 2005). Roughness at the ice-water interface increases during ice thickening, due to bubbles resting at the interface and to variations in ice thickness caused by snow depth variability on the ice surface, which modulate the conductive heat flux exiting the lake (Brown & Duguay, 2010). Increased surface roughness at the ice-water interface increases diffuse surface scattering, raising backscatter in co-polarized channels and making it the dominant return observed for freshwater ice (Engram et al., 2013b; Gunn et al., 2018). If the ice freezes to the lake bed, backscatter will be reduced because the underlying medium (e.g., gravel, soil, permafrost) absorbs most radar signals (Antonova et al., 2016; Weeks et al., 1981). Furthermore, internal structures within the lake ice, such as methane ebullition bubbles and tubular bubbles, influence the backscatter with double-bounce and single-bounce scattering (Jeffries et al., 1994; Engram et al., 2013a). Depolarizing multiple scattering events can also be caused by a high density of microscopic spherical air bubbles in surface ice types (Murfit et al., 2024; Gunn et al., 2017). Overall, the dominant source of backscattered returns from freshwater ice has been observed to be the ice-water interface, enabling the potential to retrieve LIT from radar systems (Gunn et al., 2018).

Accurate retrieval of LIT from satellite sensors remains challenging because radar signals can be affected by snow cover, ice surface, sediments, and internal structures. Early studies used an approach that indirectly determined LIT by combining detected grounded ice with lake bathymetry data for shallow lakes (Duguay & Lafleur, 2003; Hirose et al., 2008). Later, some studies recommended using a regression model from SAR backscatter. However, retrieval errors with a Root Mean Square Error (RMSE) of 11.7 cm result from the increase in roughness at the ice-water interface being uncorrelated with the growth of lake ice, particularly the quick increase in roughness during early lake ice growth (Murfit et al., 2018; Gunn et al., 2018). Data costs from in-situ training samples also limit the effectiveness of the regression method. Based on successful experiments using ground-based Frequency-Modulated Continuous-Wave (FMCW) radar on lake ice, it has been found that LIT can be derived by measuring the distance between two power peaks in range, representing the snow/ice and ice/water interfaces (Leconte et al., 2009; Gunn et al., 2015). This led to more LIT retrieval using radar altimeters on satellites such as CryoSat-2, the Jason series, and Sentinel-6 in recent years (Beckers et al., 2017; Li et al., 2022; Mangilli et al., 2024; Zhang et al., 2026).

SAR interferometry has enormous potential for LIT retrieval because it provides high-resolution mapping of microwave interactions on the order of meters, compared to radar altimetry at lower resolution (300m – 4km, depending on the sensor) (Li et al., 2022; Mangilli et al., 2024). Large numbers of shallow thermokarst lakes and small water bodies in the pan-arctic region require high-resolution observations to perform LIT mapping (Olefeldt et al., 2016). Several studies have proposed using C-band Differential Interferometric Synthetic Aperture Radar (DInSAR) to monitor LIT growth by measuring phase



65 differences across multiple SAR acquisitions (Wakabayashi et al., 2019; Siles et al., 2022; Ferguson & Gunn, 2023).
However, the accuracy of LIT retrieval using repeat-pass interferometry can be limited by low coherence, which is caused by
temporal decorrelation from the continually evolving ice-water interface during lake ice growth (Siles et al., 2022; Chen &
Gunn, 2025). Using satellite sensors with shorter repeat-pass, such as the Radarsat Constellation Mission (RCM) with under-
4-day repeat, can reduce temporal decorrelation, but lake ice deformation, such as cracks and ridges, still leads to a decrease
70 in coherence (Ferguson & Gunn, 2023). A potential solution to the temporal decorrelation impact could be to use cross-
interferometry, in which two radar sensors map the Earth's surface in the same orbit with an extremely short temporal
baseline (28 minutes for ERS-2 and ENVISAT), thereby reducing temporal decorrelation (Wegmüller et al., 2010). Recently,
the TanDEM-X pursuit monostatic mode experiment on Lac Beauséjour demonstrated high coherence on lake ice after the
Freeze-up, providing new insights for LIT retrieval using InSAR (van der Sanden et al., 2018).

75 In this study, TanDEM-X repeat-pass observations acquired in pursuit mode are used to generate interferometric height
models (Zink et al., 2014) of the ice bottom in freshwater lakes on the Alaskan North Slope. Since X-band sensors can also
penetrate ice layers and reach the ice-water interface, this study hypothesizes that elevation derived from TanDEM-X
acquisitions can retrieve LIT, with detrimental coherence effects eliminated by using data acquired in pursuit mode (Gunn et
al., 2015; Gunn et al., 2017). Objectives of this study include: (1) to derive LIT using TanDEM-X interferometry; (2) to
80 investigate the spatial-temporal pattern of lake characteristics such as grounded/float ice distributions; and (3) to compare the
LIT retrieval with in-situ measurements and simulated ice thickness using the Canadian Lake Ice Model (CLIMo) to
determine the viability of this method.

2 Study Area

LIT are retrieved for 13 thermokarst lakes in the region surrounding Utqiagvik (formerly Barrow, Alaska, 156.7674978°W,
85 71.2946711°N), located on the coast of the Arctic ocean in a region of continuous permafrost. The region is typified by a
high density of small, shallow freshwater lakes that are developed thermally through the thawing of ice-rich permafrost,
creating a basin that fills with water, forming a talik of thawed soil beneath the lake, with the elongated shape of the lakes
oriented in the prevailing wind direction (Carson & Hussey, 1962; Sturm & Liston, 2003). The lakes observed in this study
are generally shallow (average depth of 1.87m), with the maximum and minimum areas of 0.1 and 4.93 km², respectively.

90 Many lakes in this region are documented to freeze to bed annually (Surdu et al., 2015; Arp et al., 2018) during the
prolonged winter, which is an important consideration because of the impact of grounded ice on backscatter and
interferograms. Additionally, the lake ice in this area contains numerous bubbles within the ice layer (Engram et al., 2013b).
The climate surrounding Utqiagvik is influenced by its proximity to the Arctic Ocean (e.g., the presence or absence of sea
ice) and its high latitude. The climatological normal recorded at the Barrow Airport weather station (Station ID:
95 USW00027502), from 1991-2020, is typified by cool, cloudy summers with July average temperatures of 4.6 °C, and cold
winters with February average temperatures of -24.9 °C. Precipitation in Utqiagvik peaks during the summer months (July –
September) and averages approximately 157mm annually. According to climate normals, snowfall occurs in all months,



peaking in October at 0.23m, with an annual accumulation of 0.95m (ACRC, 2026). From 1949 to 2020, Utqiagvik has seen an annual increase in air temperature of 4.2 °C; the increase is even more pronounced in winter (+5.6 °C), consistent with general seasonal warming patterns associated with Arctic amplification (Box et al., 2019; ACRC, 2026).

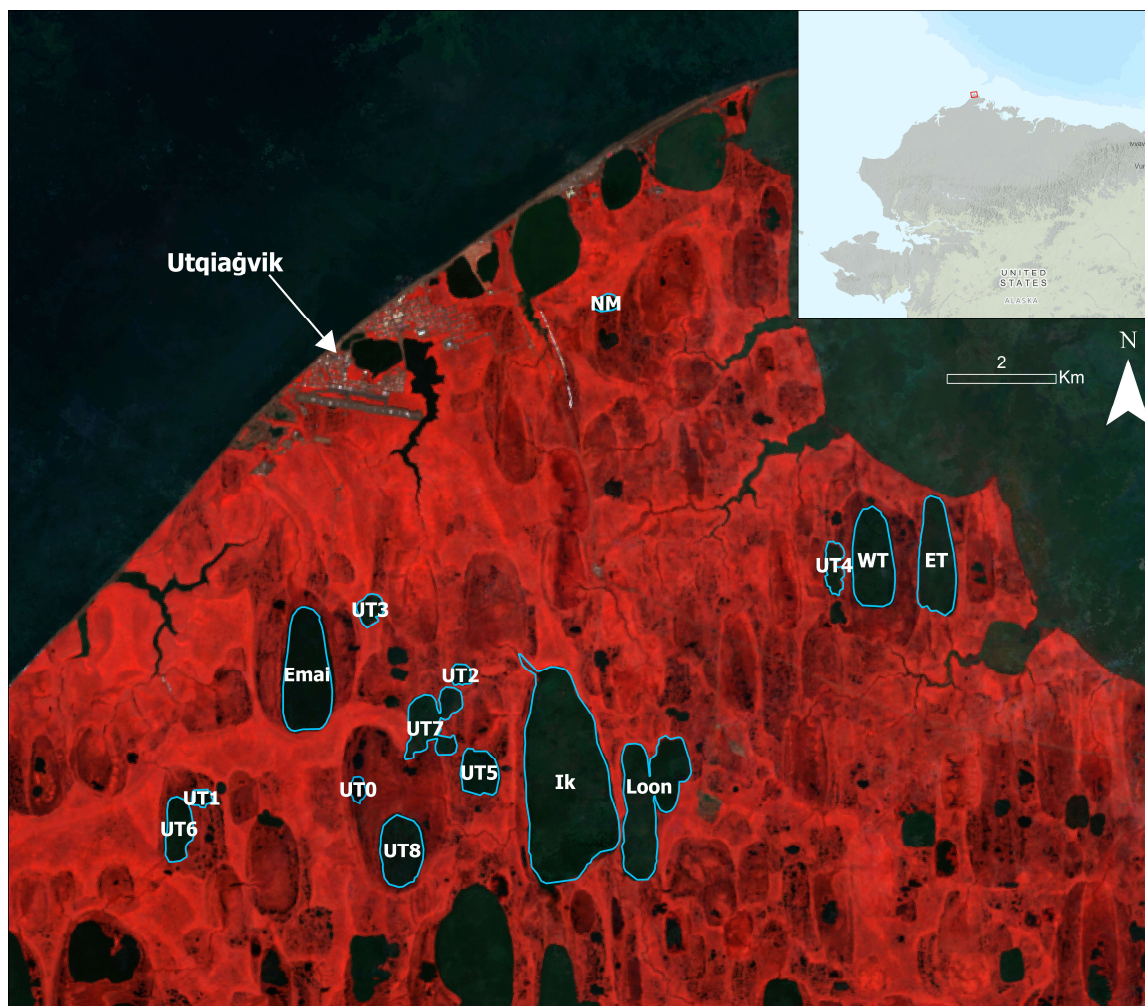


Figure 1: Freshwater lakes for ice thickness retrieval surrounding the city of Utqiagvik within the TanDEM-X acquisitions. Background images is a false colour composite from Landsat 8 derived using the median per-pixel value from an image stack extracted from 2014 – 2016 during summer months (July – September). The top-right basemap . The base map was designed and developed by Esri | Powered by Esri.

105



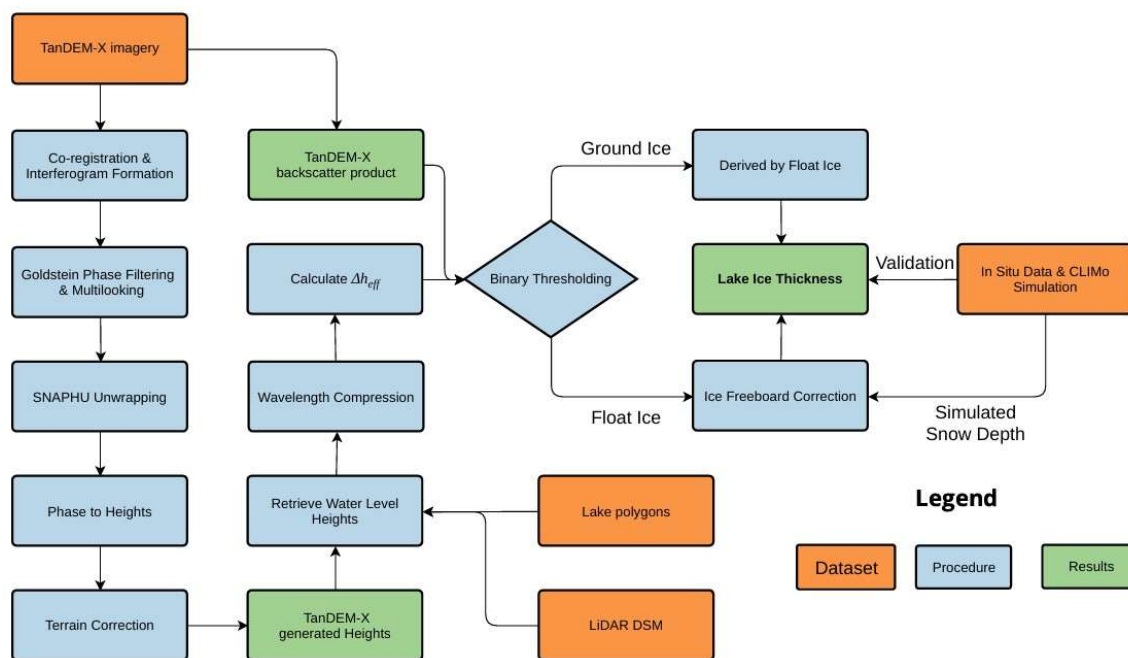
110

Table 1: The physical properties of lakes included in this study for ice thickness retrieval. Unnamed lakes are given the label UTn for subsequent result reporting, analysis, and discussion.

Lake Name	Label on Map	Area (km ²)	Average Depth (m)	Elevation a.s.l. (m)	HydroLAKES Lake ID
Ikroavik Lake	Ik	4.93	1.6	12	19674
Loon Lake	Loon	2	1.3	11	19662
Emaiksoun Lake	Emai	1.6	1.4	11	19643
West Twin Lake	WT	1.15	1.5	8	19606
East Twin Lake	ET	1.16	1.2	9	19587
North Meadow Lake	NM	0.11	1.7	14	209850
UT0	UT0	0.1	1.6	14	211072
UT1	UT1	0.1	1.7	17	211150
UT2	UT2	0.12	1.7	15	210775
UT3	UT3	0.21	2.2	15	210687
UT4	UT4	0.25	2.1	12	210425
UT5	UT5	0.48	2.1	14	210958
UT6	UT6	0.48	2.5	18	211263
UT7	UT7	0.81	2.3	14	210831
UT8	UT8	0.82	2.7	15	211256

3 Data and Methods

The procedure of LIT retrieval and validation is illustrated in the workflow presented in Figure 2. The workflow can be summarized into three parts: (1) TanDEM-X heights generation; (2) LIT retrieval from individually generated height products; and (3) accuracy assessment through comparison of in-situ observations and simulated ice thicknesses.



115

Figure 2. Workflow for estimating Lake Ice Thickness using TanDEM-X interferometry

3.1 TanDEM-X Acquisitions

The TanDEM-X mission involves two satellites, TerraSAR-X and TanDEM-X, launched by the German Aerospace Center (DLR) in 2007 and 2010, respectively. A total of 19 observations were acquired by each satellite in StripMap mode with a pursuit monostatic configuration and a short temporal separation of approximately 9-10 seconds (Table 2). The short repeat pass time results in image pairs over the Alaskan North Slope from October 2014 to February 2015. Stripmap mode acquisition provides fine spatial resolution (approximately 3 m in range and 1-3 m in azimuth). As shown in Table 2, 7 of the 19 TanDEM-X acquisitions are not appropriate for DEM generation due to the Height of Ambiguity (HoA) being too large, resulting from low perpendicular baselines between the two sensors during data acquisition.

3.2 LiDAR-derived DSM

For an accurate estimate of LIT retrieval, this study used the North Slope Borough 2018 LiDAR Digital Surface Model (DSM) dataset to retrieve elevation information; the dataset achieved a non-vegetated vertical accuracy of 4 centimetres (USGS, 2019). Additionally, the HydroLAKES dataset, providing estimated lake depth information, was used for auxiliary (Dewitz, 2020; Messenger et al., 2016).

130



Table 2. Details of TanDEM-X configurations for this study, shaded rows represent image acquisition disqualified for LIT estimation due to large HoA values. Polarization D represents a Dual-Polarized (HH+VV) image, and Q represents a Quad-Polarized image.

Acquisition Date	Time Separation (seconds)	Stripmap beam	Incidence angle range (degrees)	Perpendicular baseline (m)	HoA (m)	Polarization
10/21/2014	9.96	Stripnear 003	20 - 22	7.42	411.7	D
11/1/2014	9.97	Stripnear 003	20 - 22	11.25	271.52	D
11/12/2014	9.95	Stripnear 003	20 - 22	40.81	74.88	D
11/23/2014	9.86	Stripnear 003	20 - 22	40.57	75.29	D
12/4/2014	9.75	Stripnear 003	20 - 22	46.82	65.29	D
12/15/2014	9.77	Stripnear 003	20 - 22	135.15	22.62	D
12/20/2014	9.72	Stripnear 006	27 - 29	242.76	17.66	Q
12/26/2014	9.80	Stripnear 003	20 - 22	278.4	10.98	D
12/31/2014	9.90	Stripnear 006	27 - 29	379.53	11.29	Q
1/6/2015	9.90	Stripnear 003	20 - 22	339.26	9.01	D
1/11/2015	10.03	Stripnear 006	27 - 29	396.23	10.82	Q
1/17/2015	10.14	Stripnear 003	20 - 22	215.9	14.17	D
1/22/2015	10.2	Stripnear 006	27 - 29	182.21	23.52	Q
1/28/2015	10.24	Stripnear 003	20 - 22	88.01	34.75	D
2/2/2015	10.22	Stripnear 006	27 - 29	146.09	29.34	Q
2/8/2015	10.15	Stripnear 003	20 - 22	208.82	14.63	D
2/13/2015	10.13	Stripnear 006	27 - 29	335.56	12.06	Q
2/19/2015	10.08	Stripnear 003	20 - 22	318.09	9.61	D
2/24/2015	9.98	Stripnear 003	27 - 29	428.18	10.01	Q



3.3 TanDEM-X height generation

135 InSAR is a technology that uses multiple complex SAR images acquired at the same location to retrieve phase correlations and phase differences (Woodhouse, 2006). The phase difference between two radar acquisitions can be interpreted as a topographic displacement by taking the complex conjugate of the primary and secondary images. The interferogram is the sum of multiple phase contributions that:

$$\varphi = \varphi_{orb} + \varphi_{atm} + \varphi_{topo} + \varphi_{defo} + \varphi_{noise} \quad (1)$$

140 where φ_{orb} refers to orbital and flat earth deviation at different acquisitions, φ_{atm} is the noise due to changes of tropospheric water vapour in the atmosphere between two images, and φ_{noise} is caused by changes in the scattering characteristics of targeted objects and by thermal noise. At the same time, φ_{topo} and φ_{defo} were commonly used to retrieve elevation information and measure the surface deformation between two acquisitions (Amani et al., 2021). However, φ_{topo} and φ_{defo} don't only contain the surface information, but it might also be affected by scattering sources from upper
145 layers (Stebler et al., 2002). Because of its sensitivity to scattering from rough surfaces, VV polarization is the preferred method for detecting elevation and surface deformation. To derive surface height from an interferogram, the unwrapped interferometric phase is converted into height. The fundamental relationship links the observed phase difference φ to the height of the target relative to a reference ellipsoid (Woodhouse, 2006; ESA, 2007). The phase-to-height conversion can be expressed as:

$$150 \quad h = \phi \frac{\lambda r \sin(\theta)}{4\pi B_{\perp}} \quad (2)$$

where h is the surface height, λ is the radar wavelength, r is the slant range distance to the target, θ is the incidence angle, and B_{\perp} is the perpendicular baseline between the two satellite positions. The phase ϕ represents the unwrapped phase. A larger perpendicular baseline decreases the HoA, improving the precision of height generation. HoA represents the height difference generated by 2π phase changes, defined as:

$$155 \quad HoA = \frac{\lambda r \sin(\theta)}{2B_{\perp}} \quad (3)$$

SAR interferometry, which measures the cross-correlation between two co-registered Single Look Complex (SLC) acquisitions using their complex values to generate coherence (a measure frequently used to assess interferogram quality). Additionally, it shows how pixels in the same region have comparable physical and dielectric characteristics. According to Touzi et al. (2002), the coherence (γ) between each pixel of two SLC images, represented by the complex numbers Z_1 , Z_2 ,
160 can be mathematically expressed as follows:

$$\gamma_{(Z_1, Z_2)} = \frac{\sum_{i=1}^N (Z_1 i Z_2 i)^*}{\sqrt{\sum_{i=1}^N (Z_1 i)^2} \sqrt{\sum_{i=1}^N (Z_2 i)^2}} \quad (5)$$



where i is each sample's number, the operator $(*)$ represents the complex conjugate, and N is the total number of pixel samples. The size of the raster moving window with multiple pixels in azimuth and range determines the value N . Consequently, γ is shown as a complex number in the polar form, the phase difference is represented by the phase angle of γ , and the coherence is measured by the amplitude $|\gamma|$. The coherence value is a number between 0 and 1. If $|\gamma| = 1$, then N pixels are fully coherent, showing minimal changes in surface attributes; if $|\gamma| = 0$, then pixels are uncorrelated. Coherence values under 0.3 are often regarded as worthless for phase unwrapping and displacement measurement (Touzi et al., 2002). TanDEM-X pursuit image pairs were used to generate Height products for LIT retrieval using the Sentinel Application Platform (SNAP) from the European Space Agency (ESA). Each image acquisition was first masked to the region of interest (Utqiagvik) to improve processing efficiency, where the polarization band VV was selected for interferogram generation. The TSX and TDX images were then co-registered using 4000 ground control points (GCPs) to align each sub-pixel, reducing geometric errors to an RMS threshold of 0.001. An interferogram, along with the coherence image, was produced with the flat-Earth phase removed, while retaining the topographic phase to preserve height information (Bamler & Hartl, 1998). Goldstein filtering was applied to mitigate phase noise, using a window size of 5 and an adaptive filter exponent of 0.8 (Goldstein & Werner, 1998), followed by multi-looking to reduce remaining interferometric speckles. Phase unwrapping was performed externally using the Statistical-cost Network-flow Algorithm for Phase Unwrapping (SNAPHU) in TOPO statistical-cost mode (Chen & Zebker, 2002). The unwrapped phase was then converted to height, where range-Doppler terrain correction was applied to produce geocoded height products suitable for subsequent LIT retrieval.

3.4 LIT retrieval from Interferometry-Derived Heights

To calculate LIT from the TanDEM-X derived Height product, the hydrostatic water level height is extracted from each lake to calculate the height difference (Δh_{eff}). First, lake boundaries were obtained via high-accuracy digitization based on PlanetScope imagery and LiDAR DSM, and the buffer operation was applied to extract the surrounding terrain adjacent to each lake shoreline using a user-defined buffer distance (20 meters). For each lake, we first used the Lidar DSM to retrieve the median height difference between shoreline topography and water level, defined as h_{SW} . Then, the median of the buffered land pixels from InSAR height products was computed and identified as the shoreline height $h_{shoreline}$. The water level height was determined by subtracting the h_{SW} from $h_{shoreline}$. Height of lake ice h_{lake} was extracted for all ice pixels within the lake extent, where Δh_{eff} was calculated by subtracting the height of each lake pixel from the water level height through:

$$\Delta h_{eff} = (h_{shoreline} - h_{SW}) - h_{lake} \quad (6)$$

LIT retrieval using InSAR requires correction for the refraction of transmitted microwave through the ice from the ice surface to the ice bottom. While the electromagnetic wave travels through ice, its propagation speed decreases relative to its speed in the atmosphere due to the higher dielectric permittivity of ice. The dielectric property of ice can be described by the real part of the dielectric constant ϵ' :



$$\varepsilon'_{clear\ ice} = 3.1884 + 0.00091T \quad (7)$$

195 where T refers to the temperature of ice in Celsius; the temperature effect on the dielectric constant is negligible and can be disregarded in this study (Wegmüller et al., 2010). However, lake ice surrounding Utqiagvik typically contains numerous air bubbles within the ice layer, which alters its effective permittivity (Engram, 2013b). The dielectric constant of bubbled ice can be determined by an empirical equation based on its density:

$$\varepsilon'_{bubbled\ ice} = (1 + 0.851p)^2 \quad (8)$$

200 where p is the ice density (gcm^{-3}). Using the density of clear ice (0.917) gives a dielectric constant of 3.17 (Fujita et al., 2000). The density of bubbled lake ice has been observed to be approximately $0.85\ \text{gcm}^{-3}$, along with studies suggesting that using 90% density from pure ice for bubbled ice also leads to similar values around $0.83\ \text{gcm}^{-3}$ (Zhang et al., 2023; Murfitt et al., 2024). An ice density of $0.85\ \text{gcm}^{-3}$ is therefore used in this study which results in the dielectric constant ε' of bubbled ice around 2.97 (Fujita et al., 2000). Wavelength compression was calculated to correct the wavelength within the ice by
205 using $\varepsilon'_{bubbled\ ice} = 2.97$. The equation of wavelength compression can be described as follows, where h_{ice} is the corrected ice thickness, and θ referred to as the incidence angle in degrees (Wegmüller et al., 2010):

$$h_{ice} = \Delta h_{eff} \frac{\sqrt{\varepsilon' - \sin^2\theta}}{\varepsilon' \cos\theta} \quad (9)$$

For an incidence angle of 25 degrees, using the clear ice dielectric constant will result in a compression factor of 0.60, and 0.62 using the bubbled ice dielectric constant.

210 Additional considerations were applied for bedfast ice pixels that could interfere with the LIT inversion. The location of bedfast ice are masked, as the lakebed transmits the incoming signals through its medium, where phase information at the ice-ground is rarely returned to the sensor (Surdu et al., 2015). Hence, phase information at the bedfast ice is mainly comprised of interferometric noise or scattering objects in the upper layer of the lake ice. Bedfast ice pixels are identified using the backscatter of the VV polarization from the TanDEM-X image, derived by calibrating the SAR imagery to decibels
215 (dB), then applying the Refined Lee filter and multi-looking to reduce speckle. Similar to the study from Engram et al. 2018 for separating bedfast ice and float ice, a statistical test is first adopted to determine whether the SAR backscatter distribution within each lake was bimodal, indicating a mixture of floating and grounded ice. In such cases, a threshold was determined between the two distributions, and all pixels below this threshold were defined as bedfast ice based on Eq.10. For lakes
220 without a bimodal backscatter distribution, the median backscatter value was evaluated, and if it fell below -11 dB, the entire lake was assumed frozen to the bed. The determination of the threshold is under the assumption that a bimodal backscatter distribution is based on a two-class Gaussian Mixture Model (GMM), where the threshold can be calculated as:

$$Thres = \mu_{Bed} + \sigma_{Bed} \left(\frac{\mu_{Float} - \mu_{Bed}}{\sigma_{Float} + \sigma_{Bed}} \right) \quad (10)$$

where $Thres$ represents the determined threshold, μ_{Float} and μ_{Bed} represents the mean value of the Float ice and Bedfast ice, and σ_{Float} and σ_{Bed} are the standard deviation of two ice types. The thickness of bedfast ice was determined by calculating



225 the growth of floating ice between image acquisitions for each lake and applying that growth to grounded ice pixels that were still floating at earlier image acquisitions.

To correct the buoyant displacement of floating lake ice, an ice-freeboard calculation is applied to find the portion height of floating ice above the hydrostatic water level. The relationship between float ice thickness (T) and ice freeboard (F_i) is expressed as:

$$230 \quad F_i = \frac{T - \left(H_s \frac{\rho_s}{\rho_w - \rho_i} \right)}{\frac{\rho_w}{\rho_w - \rho_i}} \quad (11)$$

where H_s is snow depth, and ρ_w , ρ_i , and ρ_s are the densities of water, ice, and snow, respectively. In this study, densities of 1030 kgm⁻³ for water, 850 kgm⁻³ for ice, and 340 kgm⁻³ for snow were adopted based on field measurements of bubbled lake ice and typical overlying snowpack parameters for the region (Domine et al., 2012; Zhang et al., 2023). Snow depth (H_s) values were obtained from the CLIMo simulations. To assess sensitivity to snow loading, two potential freeboard estimates
235 are generated using snow cover conditions 25% and 35% from CLIMo model outputs presented in Section 4.5. Finally, the F_i were added to the original thickness T to retrieve corrected ice thickness values.

3.3 In-situ Observation

There are limited in-situ observations to use as validation for InSAR-derived LIT retrieval. The only available in-situ ice thickness observations are from the Circum Arctic Lake Observation Network (CALON), which aims to measure thicknesses
240 as they approach or reach their maximum (Arp et al., 2018). There were measurements of LIT and snow depth conducted on two of the lakes in this study, West Twin Lake and Emaiksoun on 4/7/2015, well after the last TanDEM-X image pair on 2/25/2015. These in-situ observations are used to calibrate thermodynamic ice simulations from the Canadian Lake Ice Model (CLIMo), presented in Section 4.5.

3.4 The Canadian Lake Ice Model (CLIMo)

245 Lake ice thickness is simulated for a series of mixing depth and snow cover scenarios using the Canadian Lake Ice Model (CLIMo), which is a one-dimensional thermodynamic model that has been utilized for ice phenology, composition (snow ice, clear ice) and thickness simulations for many freshwater studies in both deep and shallow lakes (Duguay et al., 2003; Brown & Duguay, 2011; Morris et al., 2005; Gunn et al., 2015). A full description of the model is provided in Ménard et al. (2002); however, the components relevant to ice thickness are provided below.

250 The surface energy budget in CLIMo is evaluated through:

$$F_0 = F_{lw} - \varepsilon\sigma T^4(0, t) + (1 - \alpha)(1 - I_0)F_{sw} + F_{lat} + F_{sens} \quad (12)$$

where F_0 is the net heat flux absorbed at the surface, ε is the surface emissivity, σ is the Stefan Boltzmann constant, T is the temperature in Kelvin, α is the surface albedo, and F_{lw} , F_{sw} , F_{lat} , and F_{sens} are the downwelling longwave, shortwave, latent, and sensible heat fluxes in Wm⁻², respectively.



255 Once frozen, ice growth at the bottom of the ice (congelation ice) is derived through the difference between the
conductive heat flux through the ice column and out of the surface of the fixed mixing layer (in this case, the lake depth),
given through:

$$\frac{\partial h_i}{\partial t} \Big|_{z=h} = \left(k \frac{\partial T}{\partial z} \Big|_{z=h} - \int_h^\infty F_{SW} I_0 (1 - \alpha) K e^{-Kz} dz \right) \frac{1}{L_{fi}} \quad (13)$$

260 where h_i is the ice thickness, k is the thermal conductivity, z is the vertical coordinate (m), I_0 is the fractional shortwave
radiation flux that penetrates through the surface, K is the bulk extinction coefficient for penetrating shortwave radiation, and
 dz is the thickness of the ice layer (Duguay et al., 2003). $\frac{1}{L_{fi}}$ is the shortwave radiation that penetrates through the bottom of
the ice column, which is assumed to be absorbed in the mixed layer and returned to the bottom of the ice. A feature of
shallow lakes, however, is that the mixed layer may also be subject to heat flux from the bottom of the lake itself, which is
treated in CLIMo with a fixed constant heat flux from the bottom. A fixed heat flux from the lake bottom is a simplification
265 that may introduce uncertainty into the LIT simulations.

CLIMo is run for all lakes where the mixing depth was set to the lake depth value from the HydroLAKES dataset; the
mixing layer depth represents the measure of heat storage in the lake. Shallow lakes are well mixed with an isothermal
temperature profile during ice-off conditions, and therefore the mixing layer depth equalling the average lake depth provides
a good approximation of the lake's temperature gradient prior to freeze-up.

270 Since the standard CLIMo formula does not explicitly constrain ice thickness growth with lake depth, we introduced a
simple geometric condition to describe the transition from floating ice to bottom-freezing ice. When simulated ice thickness
reaches the corresponding lake depth, growth of the bottom-freezing ice is set to zero. Consequently, lake ice thickness is
only permitted to increase before reaching the local lake depth, with further thickening inhibited once contact with the
bottom is established.

275 CLIMo is forced with weather data collected from a combination of available sources. Air temperature, humidity,
precipitation, and wind speed are obtained from the Barrow Airport weather station (Station ID: USW00027502). Cloud
cover fraction, a value not commonly observed at automated weather stations, was collected from the National Oceanic and
Atmospheric Administration (NOAA) Climate Data Record (CDR), specifically the Pathfinder Atmosphere Extended
(PATMOS-X) product, available in the Google Earth Engine repository (Heidinger et al., 2014). Fixed inputs to CLIMo are
280 mixing depth, dry and wet snow densities, and latitude, with dry snow density using the same values (340 kgm^{-3}) as
freeboard estimation (Domine et al., 2012). In the absence of field measurements, the empirical-based wet snow density of
 450 kgm^{-3} was applied, which will not significantly change the CLIMo simulation of this study because snow melting is
unlikely to occur on the timescale of this study (Rafat et al., 2025). Snowpacks on lakes have been documented as highly
variable, considerably more than on land, as a function of the lack of vegetation to serve as catchments and variations in
285 wind fetch from lake to lake that redistribute snow. A common approach to account for snowpack variability is to run
CLIMo with several snowfall scenarios, incorporating 0%, 25%, 35%, and 100% of the snowfall observed at the weather



station. The 0 and 100% snowfall scenarios represent the expected range of LIT that could be present, with 25% and 35% calibrated by comparing snow depth simulations with in situ measurements (Arp et al., 2018). Therefore, CLIMo is run for a total of 75 simulations across 15 lakes and 5 snow-cover scenarios.

290 3.5 Accuracy Assessment

The interferometric phase reflects the composite response of all scattering sources within the radar penetration depth (Stebler et al., 2002). While the primary contribution usually originates from the ice-water interface, additional scattering from the overlying ice layer shifts the effective phase center upward relative to the true interface. Consequently, most lake pixels for bubbled ice will underestimate LIT values. However, this phase center displacement exhibits spatial variability; regions with
295 more transparent ice or fewer inclusions allow deeper radar penetration, yielding a phase center closer to the ice-water interface. Consequently, the InSAR-derived LIT distribution within each lake should be constrained by an upper bound on actual ice thickness, with the maximum value corresponding to pixels least affected by volume scattering and phase center bias. Based on this physical interpretation, LIT is retrieved from the 99.7th percentile (3 standard deviations from the normal distribution) of each lake's LIT distribution to estimate lake-scale ice thickness, providing a robust upper-bound
300 approximation while minimizing sensitivity to noise and isolated outliers.

To evaluate the LIT accuracy, TanDEM-X-derived LITs are aggregated to the lake scale by computing the thickness at the 99.7th percentile for each lake at each image acquisition. Then, retrieved values are compared with the corresponding CLIMo-simulated ice thickness for the same lakes and dates. Accuracy assessment is performed for each lake across all temporal acquisitions using the Root Mean Square Error (RMSE), Mean Absolute Error (MAE), and Mean Bias Error
305 (MBE) (Equations 8 - 10, respectively). RMSE and MAE measure the overall magnitude of discrepancies between the satellite-derived LIT and modelled LIT, and MBE quantifies systematic over- or underestimation across lakes and dates. Three accuracy assessment metrics can be computed as:

$$RMSE = \sqrt{\frac{1}{n} \sum_{i=1}^n (P_i - O_i)^2} \quad (14)$$

310

$$MAE = \frac{1}{n} \sum_{i=1}^n |P_i - O_i| \quad (15)$$

$$MBE = \frac{1}{n} \sum_{i=1}^n (P_i - O_i) \quad (16)$$



where P_i and O_i represent the median InSAR-derived thickness and CLIMo-simulated thickness for each image acquisition i at a given lake, and n is the total number of valid TanDEM-X image acquisitions (12 for this study). Negative MBE demonstrates underestimation of LIT, and positive MBE represents overestimation.

4 Results

To constrain the snowcover scenarios for CLIMo simulations, field measurements of snow depth observation from April 7, 2015, were compared with the simulated snow conditions. Field observations from Lake Emaiksoun and West Twin Lake indicated snow depths of approximately 19.65 cm and 24 cm, respectively (Table 3). These values fall within the range of the CLIMo snowcover scenario, corresponding to 25% to 35% of the terrestrial snow depth used as atmospheric forcing in the model. This aligns with typical wind redistribution processes in Arctic Lake environments. Consequently, the CLIMo simulation scenarios employing 25% and 35% snow cover proportions were selected as the most realistic comparison scenarios for validating InSAR-derived thickness.

Table 3. Snow Depth and Ice Thickness on April 7th, 2015, from In-situ measurements and CLIMo simulations

	Lake Emaiksoun	CLIMo 25%	West Twin Lake	CLIMo 35%
Snow Depth (cm)	19.65	20	24	26
Ice Thickness (m)	1.38	1.4	1.3	1.34

Figure 3 illustrates the observed backscatter and interferometric coherence for lakes in the study region, showing that high coherence values are present for all lakes throughout the winter from the TanDEM-X image pairs, with average values exceeding the 0.3 threshold for viable interferometric analysis (Table 4). For example, the median coherence observed at the Ikroavik Lake is estimated to be around 0.95 on January 22nd 2015 (Table 4). After the ice is frozen to the lake bed, the coherence value can be impacted. In the grounded regions, the coherence values are lower than those of floating ice (Figure 3), with notable differences for all lakes with grounded ice reported in Table 4, especially for late-winter acquisitions.

Figure 4 presents the TanDEM-X-derived unwrapped phase and elevation maps for the study area. In both products, the spatial extent of the lakes can be visually distinguished from the surrounding terrain, with lake surfaces visually shown as smooth regions in the unwrapped phase map and as slightly lower elevations in the elevation map. Notably, the elevation within each lake is consistently lower than the elevations along the adjacent lakeshore. Observations across all lakes in the study region provide evidence that the TanDEM-X signal penetrates the lake ice and reflects from within the ice volume or the ice–water interface, supporting the use of TanDEM-X elevation anomalies for LIT retrieval.

Figure 5 displays the spatial distribution of InSAR-derived LIT within the 2014-2015 winter periods—early winter (December 15, 2014) and late winter (February 24, 2015). The comparison clearly shows continuous ice thickening in the study area, with an overall increase in LIT between the two observations. During early winter, most lakes exhibited thin and uniformly distributed ice cover. By late winter, the ice had not only thickened but also displayed more pronounced



heterogeneity. Given the relatively small size of the lakes studied, ice growth does not exhibit the spatial variability seen in larger lakes (Siles et al., 2022). Consequently, the depth of the lakes themselves is the primary factor determining variations in ice thickness. Notably, Loon Lake exhibited limited ice thickness, indicating ice-bed fixation where the ice layer has contacted the lake bottom, hindering further growth of the bottom ice. In contrast, deep lakes exhibited a consistent 345 thickening pattern and more pronounced spatial gradients, reflecting ongoing freeze-up under floating-ice conditions.

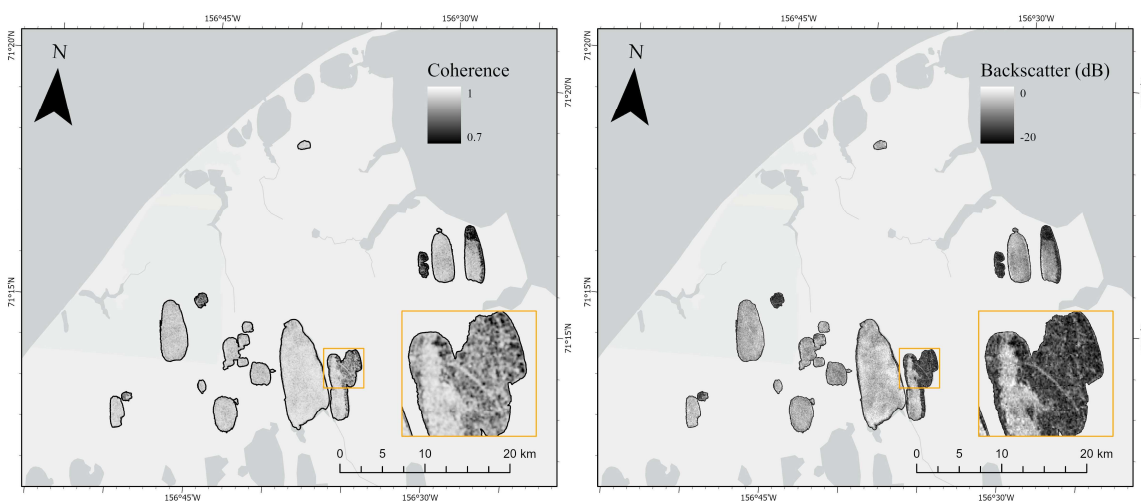
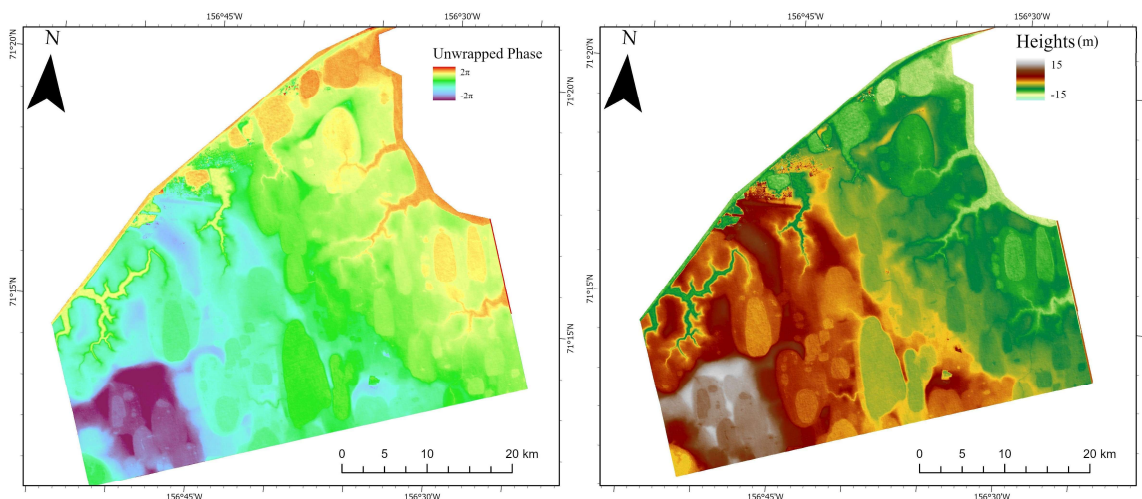


Figure 3. Coherence (left) and backscatter (right) observed at acquisition 2015-01-22, grounded Ice with darker pixel values also demonstrated lower coherence.

Table 4: Median Interferometric coherence for each lake and each image acquisition, where partially grounded lake ice is in italic and the bold represents the lake fully frozen to bed

Date	UT1	NM	UT2	UT3	UT4	UT5	UT6	UT7	UT8	WT	ET	Emai	Loon	lk
12/15/2014	0.94	0.95	0.94	0.96	0.95	0.94	0.94	0.94	0.93	0.94	0.94	0.94	<i>0.95</i>	0.95
12/20/2014	0.92	0.90	0.90	0.88	0.92	0.91	0.90	0.91	0.90	0.89	0.90	0.89	<i>0.91</i>	0.91
12/26/2014	0.89	0.90	0.84	0.85	0.90	0.86	0.88	0.87	0.85	0.88	0.89	0.86	<i>0.88</i>	0.88
12/31/2014	0.85	0.84	0.82	0.78	<i>0.83</i>	0.80	0.84	0.83	0.81	0.83	0.85	0.82	<i>0.83</i>	0.84
1/6/2015	0.86	0.86	0.81	0.81	<i>0.79</i>	0.82	0.84	0.84	0.81	0.85	0.86	0.82	<i>0.84</i>	0.86
1/11/2015	0.86	0.85	0.81	0.78	0.74	0.81	0.84	0.83	0.81	0.83	0.82	0.82	<i>0.83</i>	0.86
1/17/2015	0.90	0.93	0.90	0.86	0.82	0.91	0.91	0.92	0.90	0.92	<i>0.89</i>	0.91	<i>0.89</i>	0.93
1/22/2015	<i>0.89</i>	0.93	0.93	0.84	0.80	0.93	0.95	0.94	0.94	0.93	<i>0.90</i>	0.94	<i>0.91</i>	0.95
2/8/2015	0.83	0.92	0.91	0.86	0.82	0.90	0.92	0.91	0.91	0.94	<i>0.83</i>	0.91	<i>0.87</i>	0.93
2/13/2015	0.78	0.87	0.85	0.76	0.74	0.85	0.86	0.85	0.86	0.89	0.72	0.86	<i>0.82</i>	0.89
2/19/2015	0.76	<i>0.82</i>	0.83	0.81	0.76	0.83	0.84	0.84	0.84	0.89	0.73	0.84	<i>0.81</i>	0.88
2/24/2015	0.74	<i>0.75</i>	0.79	0.72	0.71	0.78	0.79	<i>0.79</i>	0.81	0.85	0.67	0.81	<i>0.78</i>	0.84



350 **Figure 4: Unwrapped Phase (left) and the conversion to height product (right) processed by SNAP for the region surrounding Utqiagvik, Alaska. TanDEM-X observations were acquired on December 15, 2014.**

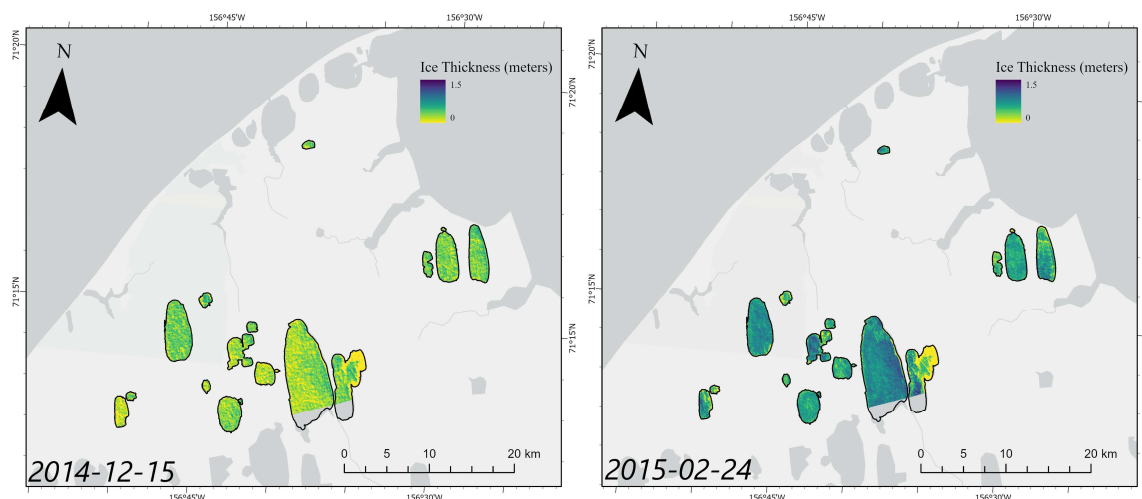


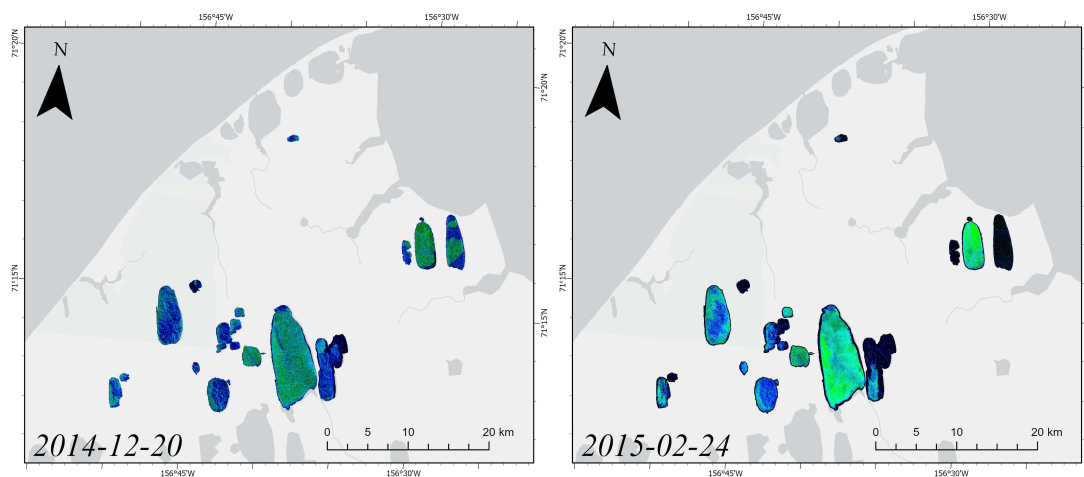
Figure 5. Maps of Estimated LIT at image acquisition of December 15, 2014 (left) and February 24, 2015 (right).

There are several Quad-polarization TanDEM-X acquisitions, which allow us for polarimetric decomposition to understand the scattering mechanisms observed over lake ice, presented in Figure 6 for early (12/20/2014) and late (2/24/2015) winter observations. Regions of surface bounce and volume scatter are presented as blue and green, respectively. Although surface bounce dominates, the contribution of volume scattering is considerable, especially during late winter (Feb 24th 2015), where the contribution of volume scattering increases in the West Twin Lake and Ikroavik Lake compared to early winter (Dec 20th

355



2014). This observed increase of volume scattering correlated with increased bubble inclusions and heterogeneity within the ice volume during ice growth, or surface ice formation (McRae-Pharo, 2025).



360

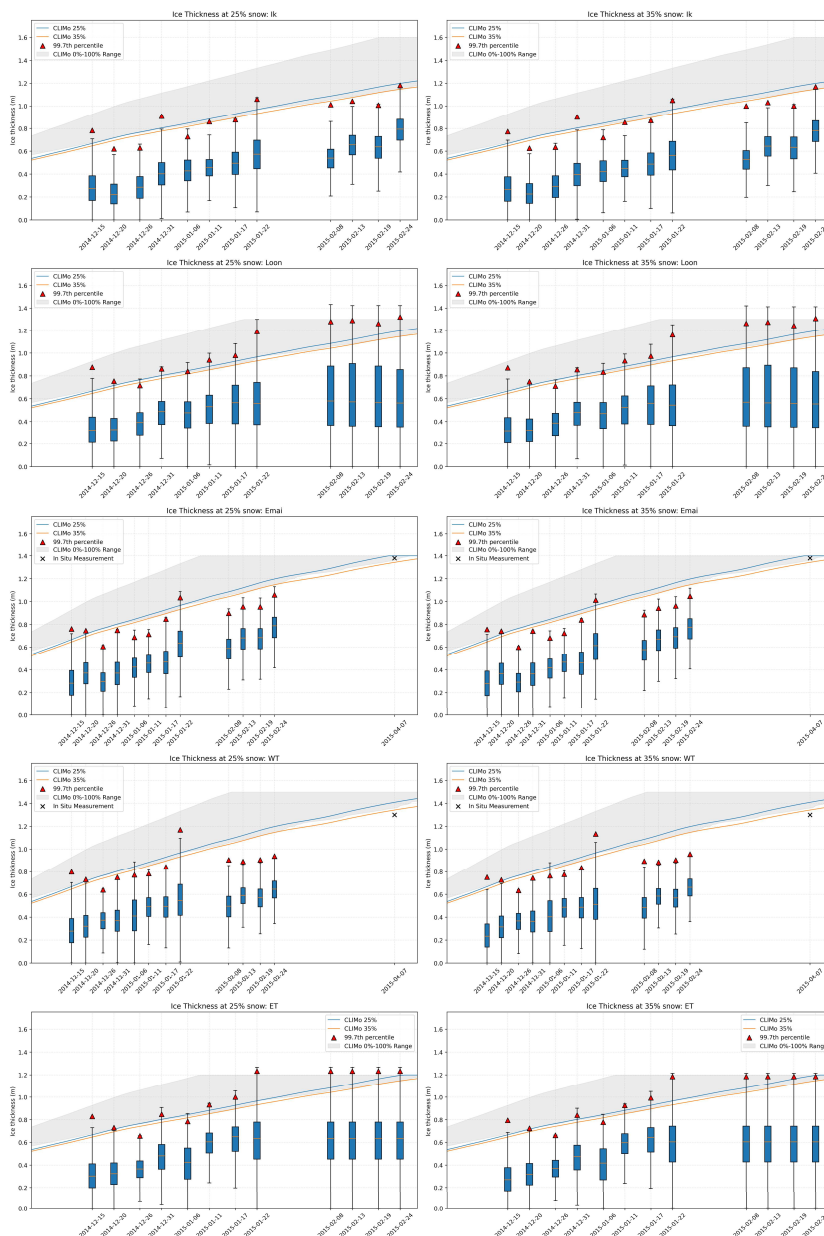
Figure 6. RGB composite (Red: Double-bounce, Green: Volume scattering, Blue: Surface-Bounce) of Freeman-Durden decomposition result between December 20, 2014 (left) and February 24, 2015 (right)

Figure 7 shows boxplots with the distribution of InSAR-derived LIT for each acquisition date for the five largest lakes in the study area and CLIMo simulations, with in-situ ice thickness measurements of West Twin Lake and Lake Emaiksoun. Due to space constraints, boxplots for the remaining lakes are provided in the supplemental materials. Due to the small difference between CLIMo simulated LIT and in situ measurements for West Twin Lake and Emaiksoun Lake, the 25% or 35% snow cover scenarios show the best agreement for comparison and accuracy assessment with our InSAR-derived thickness. Figure 8 compares InSAR-derived LIT with CLIMo simulations under 25% and 35% snow scenarios. The majority of points cluster around the 1:1 line, indicating reasonable agreement in lake ice growth. Across all dates, the median and interquartile ranges consistently fall below the simulated CLIMo thickness. Notably, the upper tail of the LIT distribution, as indicated by the 99.7th percentile, closely follows the seasonal growth pattern simulated by CLIMo.

370

Table 5 summarizes the accuracy assessment of InSAR-derived LIT relative to CLIMo simulations for the study lakes under 25% and 35% snow cover. Overall, the results show moderate agreement between InSAR estimates and simulated thicknesses, with RMSE values typically ranging from approximately 0.09 to 0.26 centimetres. MAE values are similar in magnitude, typically between 0.07 and 0.24 meters. Overall, the average RMSE for 25% and 35% snow cover scenarios is 0.186m and 0.156 respectively, with an MBE of -0.104 and -0.071 m. For most lakes, the mean bias error (MBE) is predominantly negative, indicating that InSAR systematically underestimates LIT compared to CLIMo simulations.

375



380

Figure 7. Boxplots for InSAR-derived thickness, CLIMo simulation, and in situ measurements in Ikroavik Lake, Loon Lake, Emaikousn Lake, West Twin Lake, and East Twin Lake



385

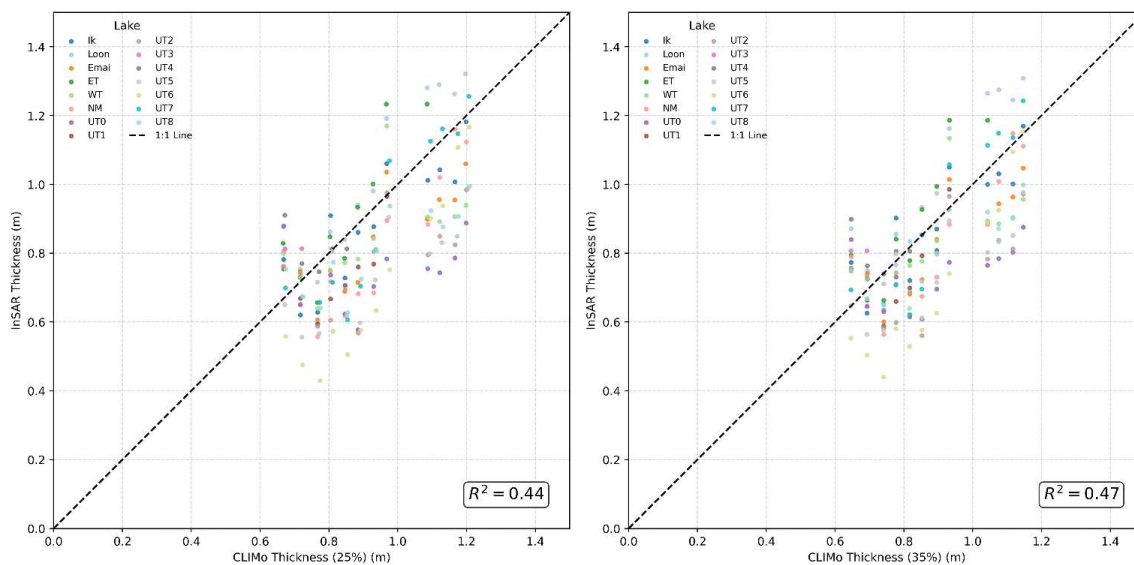


Figure 8. Scatterplot presenting InSAR-derived LIT and CLIMo simulated LIT for each lake for 25% snow (left) and 35% snow (right) scenario, lakes that are fully frozen to bed are omitted.

Table 5. Accuracy Assessment by comparing CLIMo simulations and InSAR-derived LIT for each lake across all image acquisitions.

390

Lakes	RMSE (m)		MBE (m)		MAE (m)	
	25% snow	35% snow	25% snow	35% snow	25% snow	35% snow
Ik	0.098	0.086	-0.037	-0.008	0.089	0.074
Loon	0.129	0.147	0.097	0.121	0.107	0.126
Emai	0.138	0.114	-0.094	-0.066	0.126	0.106
WT	0.163	0.134	-0.085	-0.061	0.143	0.117
ET	0.117	0.113	0.067	0.076	0.096	0.096
NM	0.156	0.127	-0.113	-0.081	0.137	0.110
UT0	0.259	0.215	-0.203	-0.164	0.238	0.196
UT1	0.244	0.190	-0.186	-0.133	0.201	0.159
UT2	0.213	0.189	-0.164	-0.137	0.185	0.168



UT3	0.212	0.184	-0.122	-0.086	0.168	0.149
UT4	0.217	0.191	-0.123	-0.091	0.172	0.149
UT5	0.221	0.180	-0.194	-0.153	0.194	0.157
UT6	0.240	0.201	-0.220	-0.176	0.219	0.177
UT7	0.112	0.101	-0.052	-0.016	0.089	0.088
UT8	0.168	0.130	-0.135	-0.094	0.148	0.111
Total	0.186	0.158	-0.104	-0.071	0.154	0.132

5 Discussion

5.1 Coherence variability across ice types

One key advantage of using TanDEM-X pursuit monostatic mode for monitoring LIT is its ability to maintain high interferometric coherence due to the extremely short revisit period (9 – 10 seconds), effectively eliminating temporal decoherence effects caused by surface changes that would occur between traditional SAR revisit periods of 4 – 12 days (Chen & Gunn, 2025; Ferguson & Gunn, 2023; Siles et al., 2022). TanDEM-X data acquired in the pursuit monostatic mode consistently maintain high coherence values on dynamic surfaces such as glacial flows and lake ice growth, which mitigate the effect of temporal decorrelation (Hong et al., 2018; van der Sanden et al., 2018). Therefore, the pursuit of the monostatic TanDEM-X technique offers methodological advantages: its sustained coherence ensures stable phase unwrapping and reliable elevation conversion throughout dynamic lake-ice processes, whereas repeat-pass InSAR methods may fail under such variable ice-surface conditions.

Previous studies using repeat-pass InSAR for LIT retrieval have shown that coherence deteriorates sharply when lake ice deformation occurs between satellite passes—particularly when cracks and ice ridges form during the time interval (Ferguson & Gunn, 2023; Siles et al., 2022). Even minor ice surface displacements or deformations driven by internal stresses disrupt the phase relationship between the two observation sets, resulting in very low coherence that limits ice thickness retrieval. On the other hand, the TanDEM-X satellite has been shown to maintain high coherence even over active deformation features such as fractures and pressure ridges. Immediate interferometry methods ensure that the scattering geometry at the ice-water interface and within ice fractures remains largely unchanged, enabling stable phase inversion even in the presence of newly formed fractures. However, despite maintaining coherence, the radar-scattering mechanism in ice cracks fundamentally differs from that in floating or grounded ice. Ice deformation may expose water or complex geometries, meaning the observed phase center does not necessarily correspond to the ice-water interface (Gunn et al., 2017; Murfitt et al., 2021). Consequently, high coherence does not guarantee that TanDEM-X thickness estimates at pressure ridges or relic leads reflect the true ice-bottom geometry, and LIT inversion results for these areas remain uncertain.



Nevertheless, the persistent high coherence indicates that TanDEM-X can still capture stable phase information related to the structural properties of the ice fracture surface. While unusable for ice thickness retrieval, the phase signal in fractured regions may offer potential for future studies through immediate interferometry, which focuses on locating deformation characteristics, fracture mechanics, or other structural properties of lake ice pertinent for ice road construction or safe travel routing.

5.2 Floating vs grounded ice

The interface between lake ice and the lake bed imposes constraints on obtaining LIT using interferometry, as the radar backscatter response is inherently weak in regions of grounded ice, reducing the reliability of phase measurements. When lake ice freezes directly onto the lake bed, lake sediments absorb the majority of SAR signals, producing only weak scattering in the X-band (Antonova et al., 2016). Consequently, SAR pixels observing bedfast ice are often dominated by noise rather than coherent echoes from a clearly defined ice-bed interface. Hence, interferometry can't directly monitor the thickness of grounded ice. During this study, grounded ice pixels are masked by testing the backscatter distribution for each lake, and the thickness values of grounded ice pixels are inverted to calculate the growth of floating ice pixels. Other approaches, such as inserting lake depth data for regions of grounded ice, are effective in shallow lake areas, but the accuracy of lake bathymetric products is a critical factor (Duguay & Lafleur, 2003). Also, it is crucial to consistently monitor lake depth to improve the LIT inversion, as lake depth and water level can change over time (Jones et al., 2023). Future research may attempt to utilize high-resolution lake bathymetric data, such as the lake bathymetric dataset generated by the Ice, Cloud, and land Elevation Satellite-2 (ICESat-2) Lidar Altimetry (Huang et al., 2025). The accuracy of grounded ice extraction can also be further validated using in-situ measurements, accounting for potential misclassification under wet-snow conditions.

5.3 Factors that affect TanDEM-X-derived accuracy

5.3.1 Height of Ambiguity

A key source of uncertainty in the TanDEM-X-derived lake ice thickness estimates arises from variations in the perpendicular baseline during image acquisitions. TanDEM-X perpendicular baselines vary because the satellites continuously adjust their relative orbits depending on mission objectives and operational constraints. The sensitivity of interferometric phase to surface height is directly proportional to the perpendicular baseline; when the baseline is small, the interferometric HoA increases, reducing the system's ability to resolve subtle vertical elevation differences (Krieger et al., 2005). As a result, DEMs generated under low-baseline conditions exhibit reduced vertical precision and are more susceptible to phase noises, residual flat-earth phase, and residual atmospheric effects. Consequently, the LIT retrieved from



DEMs using a low perpendicular baseline (<50m) may introduce errors in LIT estimation. During this study, we used TanDEM-X image acquisitions with perpendicular baselines greater than 100 meters to avoid such impacts (Table 2). This
445 resulted in HoA around 10 – 20 meters in this study, which is capable of monitoring LIT (Hong et al., 2018). However, further investigation and analysis are crucial to confirm the impact of using different vertical baselines on lake ice thickness measurements across varying regional topography.

5.3.2 Shoreline topography and water level

It is important to note that accurate LIT retrieval using the immediate interferometric method in this study is sensitive to
450 topographic effects; the precision of shoreline height estimation needs to reach the centimeter level to maintain high accuracy. This study manually digitized the lake extent to minimize such errors. However, developing automated algorithms for extracting lake boundaries is crucial for the accuracy of shoreline elevation extraction (Van der Sanden et al., 2018; Chen & Gunn, 2025). Also, this study used the LiDAR-derived DSM acquired in 2018 to estimate the height difference between water level and surrounding topography, whereas the InSAR observations used to retrieve lake ice thickness were collected
455 during the 2014-2015 winter season. Potential interannual changes in lake water levels between these periods may introduce uncertainty into the height-difference calculations, which directly affect the inferred ice thickness. Future studies would benefit from methods capable of accurately constraining lake water levels contemporaneously using altimetry, in-situ measurements, or the Surface Water and Ocean Topography (SWOT) mission designed to determine the hydrostatic level (Fu et al., 2024).

460 5.3.3 Scattering sources above the ice cover

The main limitation of the current LIT retrieval method is that using the 99.7th percentile for each lake does not guarantee the phase centre targeted at the ice-water interface. As an example, in West Twin Lake, although the mean thickness on 12/26/2014 is greater than 12/20/2014, the thickness value at the 99.7th percentile is lower (0.71 and 0.64 m, respectively). This indicates that in the former acquisition, some pixels are unaffected by scattering sources within the ice layer and reach
465 the ice-water interface, whereas in the latter image, it is likely that the phase center was observed above the ice-water interface due to scattering events. Additionally, West Twin Lake showed greater underestimation in late winter than in the early winter. This might be due to thicker ice layers, which result in more scattering events affecting the phase center. As a result, using the 99.7 percentile approach still leads to underestimating LIT at some lakes and image acquisitions due to scattering events within the ice volume.

470 On the other hand, using the 99.7th percentile leads to an overestimation of LIT in some lakes, mostly distributed at the time of image acquisition on 12/15/2014 and 1/22/2015. This might be due to the two images having a smaller perpendicular



baseline, which increases the interferometric noise, which increases the HoA (23 m compared to other acquisitions around 15 m).

5.3.4 Correction for dielectric properties in bubbled ice

475 An important consideration for InSAR-derived LIT is the dielectric permittivity assumed for wavelength compression within the ice column. While previous studies use a dielectric constant representative of clear, bubble-free freshwater ice ($\epsilon' = 3.1884$), natural lake ice often contains abundant air inclusions and internal heterogeneities that reduce the effective dielectric permittivity (Wegmuller et al., 2010). Bubble-rich ice, therefore, exhibits a lower effective ϵ' compared to clear ice, which directly influences phase-to-thickness inversion. This study adopted a reduced dielectric constant of 2.97 to
480 account for bubble inclusions, based on empirical estimates from the density of bubbled ice (Fujita et al., 2000; Zhang et al., 2023). This adjustment modifies the wavelength compression factor, resulting in estimated differences in lake ice thickness of approximately 1–3 cm. Although this magnitude may appear small relative to seasonal ice growth, it becomes considerable when monitoring LIT at high precision, such as the Global Climate Observing System (GCOS) ultimate goal of LIT uncertainty below 10 cm (GCOS 2022).

485 5.3.5 Other factors

In addition to phase-center error, although the freeboard height of floating ice with variable snow loading has been taken into account, this method did not account for the freeboard height from the snow ice formation. In the CLIMo simulation, the growth rate of the upper ice surface is extremely low, resulting in a total snow ice thickness under 1 centimetre. However, future research may consider incorporating snow ice formation to retrieve LIT. On the other hand, overestimation or
490 underestimation of LIT from CLIMo might exist, since the weather station data used in this study originate from Utqiagvik Airport; the actual atmospheric conditions over the lakes may vary slightly. Lake depth provided from the hydroLAKES dataset might be incorrect; for lake UT3 and UT4, both lakes were fully frozen to bed in the early winter season, but the dataset estimated lake depth around 2 meters, which is inconsistent with observed ice phenology, leading to our CLIMo simulation not being bounded by the actual lake depth. Additionally, CLIMo simulations might overestimate LIT in shallow
495 thermokarst lakes due to under-ice heating from taliks or lake sediments, as CLIMo adopted a fixed heat flux from the lake bottom (Rafat et al., 2023). Future analysis should integrate in-situ observations and explore the capability of TanDEM-X interferometry to monitor LIT under varying ice conditions and acquisition configurations.



5.4 Future Directions

Future advances in LIT retrieval using InSAR while ensuring high coherence should focus on better quantifying radar scattering processes within the ice column. A major source of uncertainty in InSAR-derived LIT is the displacement of the effective phase center from the ice–water interface due to volume scattering from bubble inclusions. Physically based forward modelling, such as the Snow Microwave Radiative Transfer (SMRT) framework, provides a promising approach for simulating radar interactions with layered snow and ice media and for assessing how variations in ice properties influence penetration depth and phase contributions (Picard et al., 2018; Murfitt et al., 2023). In addition, polarimetric techniques, including scattering decomposition and polarimetric interferometry (Pol-InSAR), offer the potential to separate scattering mechanisms and estimate the vertical distribution of scattering within the ice column, thereby enabling more accurate characterization of the phase center location (Cloude & Pottier, 2002). To support methodological improvements, future studies would benefit from expanded in situ measurements that document lake ice internal structure, such as bubble content and density profiles in different ice layers. Such observations are critical for parameterizing electromagnetic models, validating phase-center interpretations, and improving the physical basis of InSAR-derived lake ice thickness estimates. Beyond that, future satellite missions operating at longer wavelengths are expected to mitigate phase-center bias by reducing sensitivity to small-scale heterogeneities as they propagate through the ice cover. In particular, recently released L-band missions, such as NISAR, and the proposed TanDEM-L system are expected to improve the retrieval of lake ice thickness by enhancing sensitivity to the ice–water interface (Huber et al., 2018; Kellogg et al., 2020).

6 Conclusion

This study utilizes TanDEM-X pursuit-mode interferometry to retrieve lake ice thickness in Alaskan thermokarst lakes; the immediate interferometric method minimized temporal decorrelation, thereby reducing errors due to low coherence. By conducting an accuracy assessment of InSAR-derived thickness using CLIMo simulations and in-situ measurements, the method proposed in this study provides a framework for interferometry-derived lake ice thickness retrievals. This study maintains sufficient coherence in lake ice thickness retrieval using immediate interferometric technology and reveals that scatterers within the ice cover are another important factor affecting ice thickness retrieval. This provides a deeper understanding and additional insights for future ice thickness retrieval technology, indicating that using SAR instruments such as NISAR and TanDEM-L with longer wavelengths while maintaining high coherence has significant potential for accurate, high-resolution retrieval of lake ice thickness (Huber et al., 2018; Kellogg et al., 2020).

Future advances in LIT retrieval using InSAR should focus on better quantifying radar scattering processes within the ice column. A major source of uncertainty in InSAR-derived LIT is the displacement of the effective phase center from the ice water interface due to volume scattering from bubble inclusions. Physically based forward modelling, such as the Snow Microwave Radiative Transfer (SMRT) framework, provides a promising approach for simulating radar interactions with layered snow and ice media and for assessing how variations in ice properties influence penetration depth and phase



530 contributions (Picard et al., 2018; Murfitt et al., 2023). In addition, polarimetric techniques, including scattering
decomposition and polarimetric interferometry (Pol-InSAR), offer the potential to separate scattering mechanisms and
estimate the vertical distribution of scattering within the ice column, thereby enabling more accurate characterization of the
phase center location (Cloude & Pottier, 2002). To support methodological improvements, future studies would benefit from
expanded in-situ measurements that document lake ice internal structure, such as bubble content and density profiles in
535 different ice layers. Such observations are critical for parameterizing electromagnetic models, validating phase-center
interpretations, and improving the physical basis of InSAR-derived lake ice thickness estimates.



Figure A1

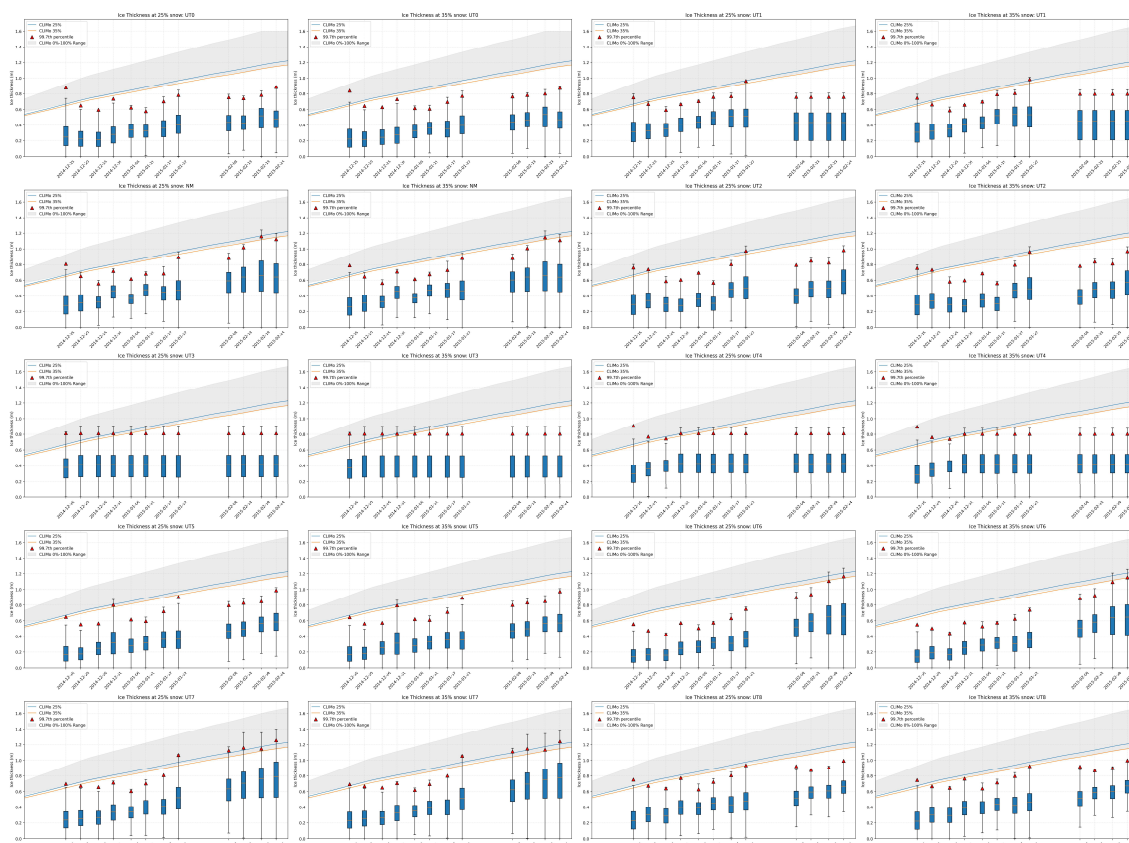


Figure A1. Boxplots for InSAR-derived thickness and CLIMo simulation in other lakes

540 Author contributions

Conceptualization, P.C. and G.G.; methodology, P.C. and G.G.; validation, P.C. and G.G.; formal analysis, P.C.; investigation, P.C.; data curation, P.C. and G.G.; writing—original draft preparation, P.C. and G.G. ; writing—review and editing, P.C. and G.G.; visualization, P.C., G.G., and S.K.; supervision, G.G.; project administration, G.G.; All authors have read and agreed to the published version of the manuscript.



545 **Data and Code Availability**

TanDEM-X data sharing is governed by licensing agreements from the German Aerospace Center (DLR). Value-added data products derived from TanDEM-X acquisitions are available upon request by the author(s) under a data sharing agreement. The code can be obtained upon request from the corresponding author.

Competing interests

550 The contact author has declared that neither of the authors has any competing interests.

Disclaimer

Copernicus Publications remains neutral with regard to jurisdictional claims made in the text, published maps, institutional affiliations, or any other geographical representation in this paper. While Copernicus Publications makes every effort to include appropriate place names, the final responsibility lies with the authors. Views expressed in the text are those of the authors and do not necessarily reflect the views of the publisher.

Acknowledgements

TanDEM-X data was accessed through the Coregistered Single look Slant range Complex (COSSC) data proposal ATI_HYDR7416 through the Science Service System (<https://tandemx-science.dlr.de/>), and original acquisitions are copyright of DLR. Thanks to Christopher Arp and Ken Hinkel providing in-situ measurements for this study.

Financial support

This research was funded by the National Science and Engineering Research Council of Canada Discovery Grant to Dr. Grant Gunn (RGPIN-2021-02742).

Review statement

565 The review statement will be added by Copernicus Publications listing the handling editor as well as all contributing referees according to their status anonymous or identified.

References

Alaska Climate Research Center: Climate normal, <https://akclimate.org/data/>, last access: 8 January 2026.



- Antonova, S., Duguay, C. R., Kääh, A., Heim, B., Langer, M., Westermann, S., and Boike, J.: Monitoring bedfast ice and ice
570 phenology in lakes of the Lena River delta using TerraSAR-X backscatter and coherence time series, *Remote Sens.*, 8, 903,
<https://doi.org/10.3390/rs8110903>, 2016.
- Amani, M., Poncos, V., Brisco, B., Foroughnia, F., DeLancey, E. R., and Ranjbar, S.: InSAR coherence analysis for
wetlands in Alberta, Canada using time-series Sentinel-1 data, *Remote Sens.*, 13, 3315, <https://doi.org/10.3390/rs13163315>,
2021.
- 575 Arp, C. D., Jones, B. M., Engram, M., Alexeev, V. A., Cai, L., Parsekian, A., Hinkel, K., Bondurant, A. C., and Creighton,
A.: Contrasting lake ice responses to winter climate indicate future variability and trends on the Alaskan Arctic Coastal
Plain, *Environ. Res. Lett.*, 13, 125001, <https://doi.org/10.1088/1748-9326/aaedb5>, 2018.
- Bamler, R. and Hartl, P.: Synthetic aperture radar interferometry, *Inverse Probl.*, 14, R1–R54, <https://doi.org/10.1088/0266-5611/14/4/001>, 1998.
- 580 Beckers, J. F., Casey, J. A., and Haas, C.: Retrievals of lake ice thickness from Great Slave Lake and Great Bear Lake using
CryoSat-2, *IEEE Trans. Geosci. Remote Sens.*, 55, 3708–3720, <https://doi.org/10.1109/TGRS.2017.2677463>, 2017.
- Box, J. E., Colgan, W. T., Christensen, T. R., Schmidt, N. M., Lund, M., Parmentier, F. J. W., Brown, R., Bhatt, U. S.,
Euskirchen, E. S., Romanovsky, V. E., and Walsh, J. E.: Key indicators of Arctic climate change: 1971–2017, *Environ. Res.
Lett.*, 14, 045010, <https://doi.org/10.1088/1748-9326/aafc1b>, 2019.
- 585 Brown, L. C. and Duguay, C. R.: The response and role of ice cover in lake–climate interactions, *Prog. Phys. Geogr.*, 34,
671–704, <https://doi.org/10.1177/0309133310375653>, 2010.
- Carson, C. E. and Hussey, K. M.: The oriented lakes of Arctic Alaska, *J. Geol.*, 70, 417–439, <https://doi.org/10.1086/626857>,
1962.
- Chen, C. W. and Zebker, H. A.: Phase unwrapping for large SAR interferograms: Statistical segmentation and generalized
590 network models, *IEEE Trans. Geosci. Remote Sens.*, 40, 1709–1719, <https://doi.org/10.1109/TGRS.2002.802453>, 2002.
- Chen, P. and Gunn, G.: Surface water extent extraction in prairie environments using Sentinel-1 image-pair coherence,
Glaciers, 2, 6, <https://doi.org/10.3390/glaciers2020006>, 2025.
- Cloude, S. R. and Pottier, E.: An entropy based classification scheme for land applications of polarimetric SAR, *IEEE Trans.
Geosci. Remote Sens.*, 35, 68–78, <https://doi.org/10.1109/36.551935>, 2002.



- 595 Dewitz, J.: National Land Cover Database (NLCD) 2016 – Alaska, U.S. Geological Survey [data set], <https://doi.org/10.5066/P96HHBIE>, 2020.
- Domine, F., Gallet, J. C., Bock, J., and Morin, S.: Structure, specific surface area and thermal conductivity of the snowpack around Barrow, Alaska, *J. Geophys. Res. Atmos.*, 117, D14114, <https://doi.org/10.1029/2011JD017429>, 2012.
- Duguay, C. R. and Lafleur, P. M.: Determining depth and ice thickness of shallow sub-Arctic lakes using space-borne optical and SAR data, *Int. J. Remote Sens.*, 24, 475–489, <https://doi.org/10.1080/0143116031000066327>, 2003.
- Duguay, C. R., Pultz, T. J., Lafleur, P. M., and Drai, D.: RADARSAT backscatter characteristics of ice growing on shallow sub-Arctic lakes, Churchill, Manitoba, Canada, *Hydrol. Process.*, 16, 1631–1644, <https://doi.org/10.1002/hyp.1010>, 2002.
- Duguay, C. R., Bernier, M., Gauthier, Y., and Kouraev, A.: Remote sensing of lake and river ice, in: *Remote Sensing of the Cryosphere*, edited by: Tedesco, M., John Wiley & Sons, Ltd., 273–306, <https://doi.org/10.1002/9781118368909.ch12>, 2015.
- 605 Engram, M., Anthony, K. W., Meyer, F. J., and Grosse, G.: Synthetic aperture radar (SAR) backscatter response from methane ebullition bubbles trapped by thermokarst lake ice, *Can. J. Remote Sens.*, 38, 667–682, <https://doi.org/10.5589/m12-060>, 2013a.
- Engram, M., Anthony, K. W., Meyer, F. J., and Grosse, G.: Characterization of L-band synthetic aperture radar (SAR) backscatter from floating and grounded thermokarst lake ice in Arctic Alaska, *The Cryosphere*, 7, 1741–1752, <https://doi.org/10.5194/tc-7-1741-2013>, 2013b.
- Engram, M., Arp, C. D., Jones, B. M., Ajadi, O. A., and Meyer, F. J.: Analyzing floating and bedfast lake ice regimes across Arctic Alaska using 25 years of space-borne SAR imagery, *Remote Sens. Environ.*, 209, 660–676, <https://doi.org/10.1016/j.rse.2018.02.022>, 2018.
- European Space Agency: *InSAR principles: guidelines for SAR interferometry processing and interpretation (TM-19, Part A)*, ESA, 2007.
- 615
- Ferguson, J. and Gunn, G. E.: Monitoring lake ice thickness growth using SAR interferometry, in: *AGU Fall Meeting Abstracts*, San Francisco, USA, December 2023, C33F-1465, 2023.
- Fu, L. L., Pavelsky, T., Cretaux, J. F., Morrow, R., Farrar, J. T., Vaze, P., and Dibarboure, G.: The surface water and ocean topography mission: A breakthrough in radar remote sensing of the ocean and land surface water, *Geophys. Res. Lett.*, 51, <https://doi.org/10.1029/2023GL107652>, 2024.
- 620



Fujita, S., Matsuoka, T., Ishida, T., Matsuoka, K., and Mae, S.: A summary of the complex dielectric permittivity of ice in the megahertz range and its applications for radar sounding of polar ice sheets, in: Physics of ice core records, Hokkaido University Press, 185–212, 2000.

625 Global Climate Observing System: The 2022 GCOS ECVs requirements (GCOS-245), World Meteorological Organization, https://meetings.wmo.int/INF06-2/InformationDocuments/INF06-2-INF06-1%2811-2%29-2022-GCOS-ECVS-REQUIREMENTS_en.pdf, last access: 28 March 2026, 2026.

Goldstein, R. M. and Werner, C. L.: Radar interferogram filtering for geophysical applications, *Geophys. Res. Lett.*, 25, 4035–4038, <https://doi.org/10.1029/1998GL900033>, 1998.

630 Gunn, G. E., Duguay, C. R., Brown, L. C., King, J., Atwood, D., and Kasurak, A.: Freshwater lake ice thickness derived using surface-based X- and Ku-band FMCW scatterometers, *Cold Reg. Sci. Technol.*, 120, 115–126, <https://doi.org/10.1016/j.coldregions.2015.09.001>, 2015.

Gunn, G. E., Duguay, C. R., Derksen, C., Clausi, D. A., and Toose, P.: Investigating the influence of variable freshwater ice types on passive and active microwave observations, *Remote Sens.*, 9, 1242, <https://doi.org/10.3390/rs9121242>, 2017.

635 Gunn, G. E., Duguay, C. R., Atwood, D. K., King, J., and Toose, P.: Observing scattering mechanisms of bubbled freshwater lake ice using polarimetric RADARSAT-2 (C-band) and UW-Scat (X- and Ku-bands), *IEEE Trans. Geosci. Remote Sens.*, 56, 2887–2903, <https://doi.org/10.1109/TGRS.2017.2786158>, 2018.

640 Hampton, S. E., Galloway, A. W. E., Powers, S. M., Ozersky, T., Woo, K. H., Batt, R. D., Labou, S. G., O'Reilly, C. M., Sharma, S., Lottig, N. R., Stanley, E. H., North, R. L., Stockwell, J. D., Adrian, R., Weyhenmeyer, G. A., Arvola, L., Baulch, H. M., Bertani, I., Bowman, L. L., and Xenopoulos, M. A.: Ecology under lake ice, *Ecol. Lett.*, 20, 98–111, <https://doi.org/10.1111/ele.12699>, 2017.

Hallikainen, M.: Dielectric properties of sea ice at microwave frequencies, NASA STI/Recon Tech. Rep. N, 78, 11293, 1977.

645 Heidinger, A., Foster, M. J., Walther, A., and Zhao, X.: NOAA Climate Data Record (CDR) of cloud properties from AVHRR Pathfinder Atmospheres-Extended (PATMOS-x), version 5.3, NOAA [data set], <https://doi.org/10.7289/V5X34VDB>, 2014.



Hirose, T., Kapfer, M., Bennett, J., Cott, P., Manson, G., and Solomon, S.: Bottomfast ice mapping and the measurement of ice thickness on tundra lakes using C-band synthetic aperture radar remote sensing, *J. Am. Water Resour. Assoc.*, 44, 285–292, <https://doi.org/10.1111/j.1752-1688.2007.00146.x>, 2008.

650 Hong, S. H., Wdowinski, S., Amelung, F., Kim, H. C., Won, J. S., and Kim, S. W.: Using TanDEM-X pursuit monostatic observations with a large perpendicular baseline to extract glacial topography, *Remote Sens.*, 10, 1851, <https://doi.org/10.3390/rs10111851>, 2018.

Huang, C. H., Zhang, S., Shah, D., Yadav, A., Li, Y., Zhao, G., and Gao, H.: 3D-LAKES: Three-dimensional global lake and reservoir bathymetry from ICESat-2 altimetry and Landsat imagery, *Sci. Data*, 12, 1625, <https://doi.org/10.1038/s41597-025-03177-5>, 2025.

655 Huber, S., de Almeida, F. Q., Villano, M., Younis, M., Krieger, G., and Moreira, A.: Tandem-L: A technical perspective on future spaceborne SAR sensors for Earth observation, *IEEE Trans. Geosci. Remote Sens.*, 56, 4792–4807, <https://doi.org/10.1109/TGRS.2018.2829057>, 2018.

660 Jeffries, M. O., Morris, K., Weeks, W. F., and Wakabayashi, H.: Structural and stratigraphic features and ERS-1 synthetic aperture radar backscatter characteristics of ice growing on shallow lakes in NW Alaska, winter 1991–1992, *J. Geophys. Res. Oceans*, 99, 22459–22471, <https://doi.org/10.1029/94JC01479>, 1994.

Jones, B. M., Kanevskiy, M. Z., Parsekian, A. D., Bergstedt, H., Ward Jones, M. K., Rangel, R. C., and Shur, Y.: Rapid saline permafrost thaw below a shallow thermokarst lake in Arctic Alaska, *Geophys. Res. Lett.*, 50, e2023GL105552, <https://doi.org/10.1029/2023GL105552>, 2023.

665 Kellogg, K., Hoffman, P., Standley, S., Shaffer, S., Rosen, P., Edelstein, W., and Sarma, C. V. H. S.: NASA-ISRO synthetic aperture radar (NISAR) mission, in: 2020 IEEE Aerospace Conference, March 2020, 1–21, <https://doi.org/10.1109/AERO47225.2020.9172542>, 2020.

Krieger, G., Fiedler, H., Hajnsek, I., Eineder, M., Werner, M., and Moreira, A.: TanDEM-X: mission concept and performance analysis, in: *IEEE International Geoscience and Remote Sensing Symposium (IGARSS)*, 4890–4893, 2005.

670 Leconte, R., Daly, S., Gauthier, Y., Yankielun, N., Bérubé, F., and Bernier, M.: A controlled experiment to retrieve freshwater ice characteristics from an FM-CW radar system, *Cold Reg. Sci. Technol.*, 55, 212–220, <https://doi.org/10.1016/j.coldregions.2008.07.005>, 2009.



- Li, X., Long, D., Huang, Q., and Zhao, F.: The state and fate of lake ice thickness in the Northern Hemisphere, *Sci. Bull.*, 67, 537–546, <https://doi.org/10.1016/j.scib.2021.12.015>, 2022.
- Mangilli, A., Duguay, C. R., Murfitt, J., Moreau, T., Amraoui, S., Mugunthan, J. S., Thibaut, P. and Donlon, C.: Improving
675 the estimation of lake ice thickness with high-resolution radar altimetry data, *Remote Sens.*, 16, 2510, <https://doi.org/10.3390/rs16142510>, 2024.
- McRae-Pharo, C.: Polarimetric decomposition of fully polarimetric synthetic aperture RADAR to examine freshwater lake ice microwave backscatter behaviour, M.Sc. thesis, University of Waterloo, <https://hdl.handle.net/10012/21669>, 2025.
- Ménard, P., Duguay, C. R., Flato, G. M., and Rouse, W. R.: Simulation of ice phenology on Great Slave Lake, Northwest
680 Territories, Canada, *Hydrol. Process.*, 16, 3691–3706, <https://doi.org/10.1002/hyp.1234>, 2002.
- Messenger, M. L., Lehner, B., Grill, G., Nedeva, I., and Schmitt, O.: Estimating the volume and age of water stored in global lakes using a geo-statistical approach, *Nat. Commun.*, 7, 13603, <https://doi.org/10.1038/ncomms13603>, 2016.
- Murfitt, J. C., Brown, L. C., and Howell, S. E.: Estimating lake ice thickness in central Ontario, *PLOS ONE*, 13, e0208519, <https://doi.org/10.1371/journal.pone.0208519>, 2018.
- 685 Murfitt, J. and Duguay, C. R.: 50 years of lake ice research from active microwave remote sensing: Progress and prospects, *Remote Sens. Environ.*, 264, 112616, <https://doi.org/10.1016/j.rse.2021.112616>, 2021.
- Murfitt, J., Duguay, C., Picard, G., and Gunn, G.: Forward modelling of synthetic aperture radar backscatter from lake ice over Canadian Subarctic lakes, *Remote Sens. Environ.*, 286, 113424, <https://doi.org/10.1016/j.rse.2022.113424>, 2023.
- Murfitt, J., Duguay, C., Picard, G., and Lemmetyinen, J.: Forward modelling of synthetic-aperture radar (SAR) backscatter
690 during lake ice melt conditions using the Snow Microwave Radiative Transfer (SMRT) model, *The Cryosphere*, 18, 869–888, <https://doi.org/10.5194/tc-18-869-2024>, 2024.
- Olefeldt, D., Goswami, S., Grosse, G., Hayes, D., Hugelius, G., Kuhry, P., McGuire, A. D., Romanovsky, V. E., Sannel, A. B. K., Schuur, E. A. G., and Turetsky, M. R.: Circumpolar distribution and carbon storage of thermokarst landscapes, *Nat. Commun.*, 7, 13043, <https://doi.org/10.1038/ncomms13043>, 2016.
- 695 Ozersky, T., Poste, A., Rautio, M., and Leu, E.: Impacts of changing winters on lake ecosystems will increase with latitude, *Ecol. Lett.*, 28, e70200, <https://doi.org/10.1111/ele.70200>, 2025.



Perrin, A., Dion, J., Eng, S., Sawyer, D., Nodelman, J. R., Comer, N., Auld, H., Sparling, E., Harris, M., Nodelman, J. Y. H., and Kinnear, L.: Economic implications of climate change adaptations for mine access roads in Northern Canada, Northern Climate ExChange, Yukon Research Centre, Yukon College, 2015.

700 Pietroniro, A. and Leconte, R.: A review of Canadian remote sensing and hydrology, 1999–2003, *Hydrol. Process.*, 19, 285–301, <https://doi.org/10.1002/hyp.5760>, 2005.

Rafat, A., Pour, H. K., Spence, C., Palmer, M. J., and MacLean, A.: An analysis of ice growth and temperature dynamics in two Canadian subarctic lakes, *Cold Reg. Sci. Technol.*, 210, 103808, <https://doi.org/10.1016/j.coldregions.2023.103808>, 2023.

705 Rafat, A., Cheng, B., and Pour, H. K.: Exploring the physics of two thermodynamic lake ice models, *Water Resour. Res.*, 61, e2024WR038615, <https://doi.org/10.1029/2024WR038615>, 2025.

Siles, G., Leconte, R., and Peters, D. L.: Retrieval of lake ice characteristics from SAR imagery, *Can. J. Remote Sens.*, 48, 379–399, <https://doi.org/10.1080/07038992.2021.1960586>, 2022.

710 Simpson, C. E., Arp, C. D., Sheng, Y., Carroll, M. L., Jones, B. M., and Smith, L. C.: Landsat-derived bathymetry of lakes on the Arctic Coastal Plain of northern Alaska, *Earth Syst. Sci. Data*, 13, 1135–1150, <https://doi.org/10.5194/essd-13-1135-2021>, 2021.

Stebler, O., Meier, E., and Nüesch, D.: Multi-baseline polarimetric SAR interferometry—first experimental spaceborne and airborne results, *ISPRS J. Photogramm. Remote Sens.*, 56, 149–166, [https://doi.org/10.1016/S0924-2716\(02\)00142-4](https://doi.org/10.1016/S0924-2716(02)00142-4), 2002.

715 Sturm, M. and Liston, G. E.: The snow cover on lakes of the Arctic Coastal Plain of Alaska, USA, *J. Glaciol.*, 49, 370–380, <https://doi.org/10.3189/172756503781830539>, 2003.

Surdu, C. M., Duguay, C. R., Pour, H. K., and Brown, L. C.: Ice freeze-up and break-up detection of shallow lakes in Northern Alaska with spaceborne SAR, *Remote Sens.*, 7, 6133–6159, <https://doi.org/10.3390/rs70506133>, 2015.

Touzi, R., Lopes, A., Bruniquel, J., and Vachon, P. W.: Coherence estimation for SAR imagery, *IEEE Trans. Geosci. Remote Sens.*, 37, 135–149, <https://doi.org/10.1109/36.739146>, 2002.

720 U.S. Geological Survey: 2018 USGS lidar: North Slope Borough communities, AK – QL1 and QL2, NOAA [data set], <https://www.fisheries.noaa.gov/inport/item/63140>, 2019.



- van der Sanden, J. J., Short, N. H., and Drouin, H.: InSAR coherence for automated lake ice extent mapping: TanDEM-X bistatic and pursuit monostatic results, *Int. J. Appl. Earth Obs. Geoinf.*, 73, 605–615, <https://doi.org/10.1016/j.jag.2018.07.015>, 2018.
- 725 Vincent, L. A., Wang, X. L., Milewska, E. J., Wan, H., Yang, F., and Swail, V.: A second generation of homogenized Canadian monthly surface air temperature for climate trend analysis, *J. Geophys. Res. Atmos.*, 117, D18110, <https://doi.org/10.1029/2012JD017859>, 2012.
- Wakabayashi, H., Motohashi, K., and Maezawa, N.: Monitoring lake ice in northern Alaska with backscattering and interferometric approaches using Sentinel-1 SAR data, in: IGARSS 2019 – 2019 IEEE International Geoscience and Remote Sensing Symposium, Yokohama, Japan, 28 July–2 August 2019, 4202–4205, <https://doi.org/10.1109/IGARSS.2019.8899364>, 2019.
- 730 Weeks, W. F., Gow, A. J., and Schertler, R. J.: Ground-truth observations of ice-covered North Slope lakes imaged by radar, CRREL Rep. 81-19, U.S. Army Cold Regions Research and Engineering Laboratory, Hanover, New Hampshire, USA, 1981
- Wegmüller, U., Santoro, M., Werner, C., Strozzi, T., and Wiesmann, A.: Estimation of ice thickness of tundra lakes using ERS-ENVISAT cross-interferometry, in: 2010 IEEE International Geoscience and Remote Sensing Symposium, Honolulu, HI, USA, 25–30 July 2010, 316–319, <https://doi.org/10.1109/IGARSS.2010.5649507>, 2010.
- 735 West, L. J., Rippin, D. M., Murray, T., Mader, H. M., and Hubbard, B.: Dielectric permittivity measurements on ice cores: implications for interpretation of radar to yield glacial unfrozen water content, *J. Environ. Eng. Geophys.*, 12, 37–45, <https://doi.org/10.2113/JEEG12.1.37>, 2007.
- 740 Zink, M., Bachmann, M., Bräutigam, B., Fritz, T., Hajnsek, I., Moreira, A., and Krieger, G.: TanDEM-X: The new global DEM takes shape, *IEEE Geosci. Remote Sens. Mag.*, 2, 8–23, <https://doi.org/10.1109/MGRS.2014.2318895>, 2014.
- Zhang, M., Chen, F., Guan, W., and Zhao, H.: Rapid thinning of lake ice for Himalayan glacial lakes since 2010, *Remote Sens. Environ.*, 332, 115062, <https://doi.org/10.1016/j.rse.2025.115062>, 2026.
- 745 Zhang, Y., Fregona, M., Loehr, J., Ala-Könni, J., Song, S., Leppäranta, M., and Li, Z.: A field study on ice melting and breakup in a boreal lake, Pääjärvi, in Finland, *The Cryosphere*, 17, 2045–2058, <https://doi.org/10.5194/tc-17-2045-2023>, 2023.